EUROPEAN JOURNAL OF PURE AND APPLIED MATHEMATICS
2026, Vol. 19, Issue 2, Article Number 7627
ISSN 1307-5543 – ejpam.com
Published by New York Business Global

Approximate Localized Waves and Residual Diagnostics for a Damped Nonplanar Time–Fractional Korteweg–de Vries Equation

Álvaro H. Salas S.

Department of Mathematics and Statistics, Universidad Nacional de Colombia, Sede Manizales, Manizales, Colombia; FIZMAKO Research Group

Abstract. This paper studies a damped nonplanar time-fractional Korteweg–de Vries equation with Caputo memory, quadratic convection, dispersion, linear damping, and geometric attenuation. A family of localized analytical predictors is constructed by combining classical KdV profiles with a fractional time deformation and a Mittag–Leffler/nonplanar attenuation law. Since the Caputo operator does not satisfy a classical product rule and the nonplanar coefficient is singular at the initial time, the resulting profiles are not claimed to be exact solutions. Instead, their consistency is assessed by explicit residual diagnostics on truncated time intervals. The Caputo derivative is evaluated by a graded-mesh L1 history formula, and Chebyshev reconstruction is also discussed as a complementary diagnostic tool. Representative planar, damped, and cylindrical benchmarks show that the residual remains small and coherent in planar regimes, while nonplanar geometry amplifies the early-time mismatch but becomes more controlled at later times. The approach provides a transparent residual-based framework for studying memory, damping, and geometric effects in fractional KdV dynamics.

2020 Mathematics Subject Classifications: 35Q53, 35R11, 26A33, 65M06, 65M70

Key Words and Phrases: Caputo derivative, time-fractional Korteweg–de Vries equation, nonplanar KdV equation, localized waves, residual diagnostics, Mittag–Leffler attenuation

1. Introduction

The Korteweg–de Vries (KdV) equation is one of the fundamental nonlinear evolution equations for the description of weakly nonlinear and weakly dispersive waves. Since its classical derivation for long waves in shallow water [1], it has played a central role in applied mathematics and mathematical physics, with important applications in fluid mechanics, plasma physics, internal waves, and other dispersive media. Its significance stems from the balance between quadratic nonlinearity and third-order dispersion, which allows the emergence of coherent structures such as solitary waves and other long-lived patterns [2–4].

DOI: https://doi.org/10.29020/nybg.ejpam.v19i2.7627

Email address: ahsalass@unal.edu.co (A. H. Salas S.)

In many realistic situations, however, the standard KdV equation is not sufficient to describe the observed dynamics. Physical media often exhibit dissipation, relaxation, and geometric spreading. Damping may arise from viscosity, friction, collisional effects, or radiative losses, whereas nonplanar propagation modifies wave evolution through geometric expansion effects. In cylindrical and spherical settings, these effects lead to additional attenuation and produce nonautonomous corrections to the standard KdV balance [5, 6]. As a consequence, the resulting wave dynamics may differ substantially from those predicted by the classical planar model.

A further level of complexity appears when the medium possesses memory. In that case, the present state depends not only on the instantaneous configuration but also on the past history of the system. Fractional calculus provides a natural framework for incorporating such hereditary effects. Among the available fractional operators, the Caputo derivative is especially convenient in applications because it preserves the use of standard initial conditions while introducing nonlocal temporal memory through a weakly singular kernel [7–10]. Fractional models have therefore become important in the study of anomalous transport, viscoelasticity, wave propagation in complex media, and related phenomena.

Motivated by these developments, time-fractional versions of nonlinear wave equations, including KdV-type models, have received increasing attention [11–13]. Replacing the first-order time derivative by a Caputo derivative of order $0 < \alpha < 1$ changes the temporal response in a fundamental way: classical exponential relaxation is replaced by Mittag–Leffler-type behavior, and the subsequent evolution becomes history dependent. This substantially increases both the analytical and numerical difficulty of the problem, especially over long time intervals. Recent studies also show that fractional nonlinear models continue to attract considerable interest in neighboring areas such as fractional dispersive transport, nonlinear optical structures, generalized viscous-capillarity models, and related wave systems [14–19]. These contributions further underline the importance of mathematically consistent formulations and reliable computational diagnostics for fractional nonlinear evolution equations.

In this paper, we consider a damped nonplanar time-fractional Korteweg–de Vries equation of the form

$$ {}^{C}D_t^{\alpha}u(x,t) + \mu\, u(x,t)u_x(x,t) + \nu\, u_{xxx}(x,t) + \left(\frac{\kappa}{2t} + \delta\right) u(x,t) = 0, \qquad 0 < \alpha < 1. $$

Here, ${}^{C}D_t^{\alpha}u$ denotes the Caputo fractional derivative in time, $\mu\, uu_x$ is the nonlinear convective term, $\nu\, u_{xxx}$ is the dispersive contribution, and δu represents linear damping. The additional term $\frac{\kappa}{2t}u$ models the attenuation associated with nonplanar propagation through an explicitly time-dependent geometric factor. The values $\kappa = 0$, $\kappa = 1$, and $\kappa = 2$ correspond, respectively, to planar, cylindrical, and spherical geometries. From a modeling viewpoint, the equation combines nonlinear KdV propagation, dissipative effects, nonplanar geometric attenuation, and fractional temporal memory within a single nonautonomous framework.

The main challenge in the analysis of this model is the combined presence of nonlocal memory and nonautonomous attenuation. In contrast with the classical case, the Caputo

operator requires the full time history of the solution, which increases computational cost and may reduce accuracy if the discretization is not handled carefully. At the same time, the coefficient $\kappa/(2t)$ introduces a singular behavior near the initial time, so the early-time regime requires particular care both analytically and numerically. These features complicate the interpretation of approximate localized profiles and the design of stable computational procedures.

For this reason, the present work adopts a deliberately cautious viewpoint. Rather than claiming an exact closed-form treatment of the full damped nonplanar fractional equation, we construct a localized analytical predictor intended to capture the combined qualitative influence of memory, damping, and nonplanar geometry on wave attenuation. This predictor is then assessed through explicit residual diagnostics and numerical comparisons. The Caputo derivative is treated in the numerical section with clearly stated discrete weights, while auxiliary reconstructions are used to examine the behavior of the resulting approximations over finite time intervals. The emphasis is therefore placed on internal consistency between the model, the approximation framework, and the interpretation of the computed solutions.

The objectives of the paper are twofold. First, we investigate how the fractional order, the damping coefficient, and the nonplanar parameter affect attenuation, dispersion, and wave persistence in planar, cylindrical, and spherical settings. Second, we examine the consistency of a residual-based approximation strategy for this class of fractional KdV-type problems. In this way, the paper aims to provide a coherent and transparent analytical–numerical study without overstating claims of exact solvability or methodological novelty.

The remainder of the paper is organized as follows. Section 2 introduces the analytical background and the localized predictor used in the study. Section 3 presents the numerical formulation, including the Caputo discretization and the residual diagnostics employed in the computations. Section 4 reports representative numerical results and discusses the effects of the main parameters. Finally, Section 5 summarizes the main conclusions and outlines possible directions for future work.

2. Preliminaries

2.1. Mittag–Leffler Functions

The one–parameter Mittag–Leffler function, which plays a central role in fractional relaxation and evolution processes [20, 21], is defined by

$$E_\alpha(z) = \sum_{k=0}^{\infty} \frac{z^k}{\Gamma(\alpha k + 1)}, \qquad \alpha > 0, \tag{1}$$

and generalizes the exponential function, since $E_1(z) = e^z$. The two–parameter Mittag–Leffler function

$$E_{\alpha,\beta}(z) = \sum_{k=0}^{\infty} \frac{z^k}{\Gamma(\alpha k + \beta)}, \qquad \alpha > 0,\ \beta > 0, \tag{2}$$

naturally appears as the resolvent kernel of fractional evolution equations. For $0 < \alpha < 1$, the function $E_\alpha(-\lambda t^\alpha)$ decays algebraically, reflecting the long–memory effects induced by fractional derivatives.

2.2. Caputo Fractional Derivative

For $0 < \alpha < 1$, the Caputo derivative of a sufficiently smooth function $u(t)$ is

$$ {}^{C}D_t^{\alpha} u(t) = \frac{1}{\Gamma(1-\alpha)} \int_0^t \frac{u'(\tau)}{(t-\tau)^{\alpha}}\, d\tau. \tag{3}$$

It preserves classical initial conditions and is therefore well suited for physical applications; standard references include [8–10, 22].

2.3. Model Equation

In this work, we consider the damped nonplanar time–fractional Korteweg–de Vries equation

$$ {}^{C}D_t^{\alpha} u + \mu\, u u_x + \nu\, u_{xxx} + \left(\frac{\kappa}{2t} + \delta\right) u = 0, \qquad 0 < \alpha < 1. \tag{4}$$

Here, ${}^{C}D_t^{\alpha} u$ denotes the Caputo fractional derivative in time, $\mu\, u u_x$ is the quadratic nonlinear term, $\nu\, u_{xxx}$ is the dispersive contribution, δu represents linear damping, and $\frac{\kappa}{2t} u$ models the attenuation induced by nonplanar propagation. The values $\kappa = 0$, $\kappa = 1$, and $\kappa = 2$ correspond, respectively, to planar, cylindrical, and spherical geometries.

A central difficulty in (4) is that the geometric coefficient $\kappa/(2t)$ is singular at $t = 0$. For this reason, the approximate profiles introduced below are interpreted on truncated time intervals

$$ t \in [t_{\min}, T], \qquad t_{\min} > 0, \tag{5}$$

rather than in the singular initial-time regime.

3. Residual Evaluation and Numerical Approximation of the Caputo Derivative

Our approach does not rely on parameter minimization. Instead, we evaluate the residual

$$ R(x,t;\rho) = {}^{C}D_t^{\rho} U + \mu\, U U_x + \nu\, U_{xxx} + \left(\frac{\kappa}{2t} + \delta\right) U, \qquad 0 < \rho < 1, \tag{6}$$

where $U(x,t)$ is an analytically motivated approximate profile. The main numerical difficulty in (6) is the reliable evaluation of the Caputo derivative, especially near the initial time, where fractional solutions often exhibit weak singular behavior.

3.1. Graded-Mesh L1 Approximation of the Caputo Derivative

In the present work, the fractional order satisfies

$$0 < \rho < 1.$$

Accordingly, the Caputo derivative of a sufficiently regular function $u(t)$ is defined by

$$ {}^{C}D_t^{\rho} u(t) = \frac{1}{\Gamma(1-\rho)} \int_0^t \frac{u'(\tau)}{(t-\tau)^{\rho}}\, d\tau. \tag{7}$$

This operator is nonlocal in time: its value at t depends on the entire past history of the solution. Moreover, the kernel $(t-\tau)^{-\rho}$ is weakly singular near $\tau = t$, and many fractional evolution problems also display weak singular behavior near $t = 0$. For these reasons, a uniform time discretization may lose accuracy near the origin. To overcome this difficulty, we employ a graded temporal mesh together with the classical L1 approximation, a standard history-based discretization in fractional differential equations [13, 23–25].

3.1.1. Graded temporal mesh

Let $T > 0$ be the final time and let N be the number of time subintervals. We define the nonuniform temporal nodes by

$$t_j = T\left(\frac{j}{N}\right)^{\gamma}, \qquad j = 0, 1, \ldots, N, \tag{8}$$

where $\gamma \geq 1$ is the grading exponent. When $\gamma = 1$, the grid is uniform; when $\gamma > 1$, the nodes are concentrated near $t = 0$. This clustering is designed to improve the numerical resolution of the initial-time singularity.

3.1.2. Splitting the memory integral into time slabs

We wish to approximate ${}^{C}D_t^{\rho} u(t_i)$ at the mesh points t_i. Splitting the integral in (7) over the subintervals of the graded mesh gives

$$\begin{aligned} {}^{C}D_t^{\rho} u(t_i) &= \frac{1}{\Gamma(1-\rho)} \int_0^{t_i} \frac{u'(\tau)}{(t_i-\tau)^{\rho}}\, d\tau \\ &= \frac{1}{\Gamma(1-\rho)} \sum_{j=0}^{i-1} \int_{t_j}^{t_{j+1}} \frac{u'(\tau)}{(t_i-\tau)^{\rho}}\, d\tau. \end{aligned} \tag{9}$$

Thus the memory term is decomposed into a sum of history contributions over all previous time intervals.

3.1.3. Piecewise linear approximation of the derivative

On each interval $[t_j, t_{j+1}]$, we approximate $u'(\tau)$ by the slope of the linear interpolant between the endpoint values:

$$u'(\tau) \approx \frac{u(t_{j+1}) - u(t_j)}{t_{j+1} - t_j}, \qquad \tau \in [t_j, t_{j+1}]. \tag{10}$$

This approximation has two practical advantages. First, it uses only nodal values of u, so no explicit derivative such as $u'(0)$ is required. Second, once (10) is substituted into (9), the singular kernel can still be integrated exactly.

Substituting (10) into (9) yields

$${}^{C}D_t^{\rho} u(t_i) \approx \frac{1}{\Gamma(1-\rho)} \sum_{j=0}^{i-1} \frac{u(t_{j+1}) - u(t_j)}{t_{j+1} - t_j} \int_{t_j}^{t_{j+1}} (t_i - \tau)^{-\rho}\, d\tau. \tag{11}$$

3.1.4. Exact integration of the kernel

The kernel integral in (11) can be evaluated explicitly:

$$\int_{t_j}^{t_{j+1}} (t_i - \tau)^{-\rho}\, d\tau = \frac{(t_i - t_j)^{1-\rho} - (t_i - t_{j+1})^{1-\rho}}{1-\rho}. \tag{12}$$

Using the Gamma identity

$$\Gamma(2-\rho) = (1-\rho)\Gamma(1-\rho),$$

we obtain the graded-mesh L1 approximation

$${}^{C}D_t^{\rho} u(t_i) \approx \sum_{j=0}^{i-1} \Phi_{i,j} \left[u(t_{j+1}) - u(t_j)\right], \qquad i = 1, 2, \ldots, N, \tag{13}$$

where the weights are defined by

$$\Phi_{i,j} = \frac{(t_i - t_j)^{1-\rho} - (t_i - t_{j+1})^{1-\rho}}{\Gamma(2-\rho)\,(t_{j+1} - t_j)}. \tag{14}$$

This is the Caputo discretization used throughout the numerical experiments of the present work.

3.1.5. Equivalent interpretation

Formula (13) shows that the Caputo derivative is approximated as a weighted sum of all past increments

$$u(t_{j+1}) - u(t_j).$$

Each increment measures the change of the solution over one time interval, while the corresponding coefficient $\Phi_{i,j}$ determines how strongly that past change influences the present time t_i. Since the weights decay algebraically, recent changes contribute more strongly than distant ones, but the memory of the older history is never completely lost.

3.1.6. Interpretation in plain language

It is useful to summarize the meaning of the scheme in simple terms.

- The Caputo derivative measures how the current state depends on the entire past.
- On each interval $[t_j, t_{j+1}]$, the method estimates the local temporal change using only the two function values $u(t_j)$ and $u(t_{j+1})$.
- These local changes are then accumulated with algebraically decaying memory weights.
- The graded mesh places more points near $t = 0$, where fractional solutions are usually most delicate.

Thus the method avoids unstable derivative evaluations at the origin while preserving the essential memory structure of the Caputo operator.

3.1.7. Accuracy and behavior near the origin

For sufficiently smooth solutions, the L1 approximation is well known to provide reliable convergence. However, in fractional evolution problems the solution often has weak singular behavior near $t = 0$, and this may reduce the observed rate on a uniform mesh. The graded discretization (8) compensates for this by refining the mesh near the origin, thereby improving both accuracy and stability in the early-time regime.

In practice, the grading exponent γ is chosen according to the strength of the singularity. Larger values of γ produce stronger clustering near $t = 0$ and therefore better resolution of initial transients.

3.1.8. Advantages of the graded-mesh L1 approximation

The main advantages of the present discretization are the following.

- *No explicit derivatives are required*: the method depends only on function values.
- *Stable near the origin*: the graded mesh is well suited to weakly singular fractional solutions.
- *Exact kernel integration*: the Caputo kernel is integrated analytically on each time slab.
- *Simple implementation*: the final formula is an explicit history sum with closed-form weights.
- *Appropriate for residual evaluation*: the method is robust and easy to apply to candidate approximate profiles.

3.1.9. How it is used in the residual evaluation

In the residual computations, formula (13) is applied at each spatial grid point $x = x_\ell$ to the time history

$$\{U(x_\ell, t_j)\}_{j=0}^{i}.$$

This yields a numerical approximation of ${}^{C}D_t^{\rho}U(x_\ell, t_i)$, which is then combined with the nonlinear, dispersive, damping, and nonplanar terms in (6). In this way, the residual can be evaluated directly from the candidate profile $U(x,t)$ without constructing a full time-marching solver.

Table 1: Main features of the graded-mesh L1 approximation for $0 < \rho < 1$.

Feature	**Description**
Fractional order	$0 < \rho < 1$
Underlying idea	Piecewise linear approximation of the temporal variation on each subinterval
Temporal grid	Nonuniform graded mesh with node concentration near $t = 0$
Discrete data required	Function values $u(t_j)$ only
Kernel treatment	Exact integration of the Caputo kernel over each subinterval
Behavior near $t = 0$	Improved stability and accuracy for weakly singular solutions
Implementation	Explicit history sum with closed-form weights
Recommended use	Residual evaluation and numerical verification for fractional models

4. Formal Approximate Profiles Generated from Classical KdV Solutions

Rather than seeking exact closed-form solutions of the full nonautonomous fractional model (4), we use known solutions of the classical KdV equation as reference profiles and modulate them by a time-dependent attenuation factor. This provides a formal approximation that captures, at leading order, the combined influence of fractional memory, damping, and nonplanar geometric attenuation.

4.1. Classical KdV Reference Equation

Let $U(x,\tau)$ be a solution of the classical Korteweg–de Vries equation

$$U_\tau + \mu\, U U_x + \nu\, U_{xxx} = 0. \tag{15}$$

This equation provides the spatial templates used in the sequel, including solitary waves, multi-soliton configurations, and periodic traveling-wave solutions.

4.2. Fractional Time Reparametrization

A natural way to connect the classical KdV dynamics with the time–fractional model (4) is through the fractional time variable

$$\tau(t) = \frac{t^\alpha}{\Gamma(1+\alpha)}, \tag{16}$$

which reduces to the classical time t in the limit $\alpha \to 1$. This reparametrization is consistent with the well-known role of $\frac{t^\alpha}{\Gamma(1+\alpha)}$ in fractional evolution problems and provides a convenient way to transplant classical KdV wave forms into the fractional setting.

4.3. Formal Amplitude Modulation

We seek an approximate solution of (4) in the form

$$u_{\text{app}}(x,t) = A(t)\, U(x, \tau(t))\,, \qquad t \geq t_{\min} > 0, \tag{17}$$

where U solves (15) and $A(t)$ is a scalar attenuation factor to be chosen.

Substituting (17) formally into (4) suggests that, at leading order, the amplitude should satisfy

$$^C D_t^\alpha A(t) + \left(\frac{\kappa}{2t} + \delta\right) A(t) \approx 0. \tag{18}$$

Because of the explicitly singular coefficient $\kappa/(2t)$, equation (18) is not treated here as an exact closed-form amplitude equation on $[0, T]$. Instead, we use a leading-order attenuation law consistent with the fractional damping factor and the nonplanar geometric decay:

$$A(t) \approx t^{-\kappa/2} E_\alpha(-\delta t^\alpha), \qquad t \geq t_{\min} > 0. \tag{19}$$

This leads to the formal approximate profile

$$u_{\text{app}}(x,t) \approx t^{-\kappa/2} E_\alpha(-\delta t^\alpha)\, U\left(x, \frac{t^\alpha}{\Gamma(1+\alpha)}\right), \qquad t \geq t_{\min} > 0. \tag{20}$$

4.4. Interpretation and Range of Validity

Approximation (20) should be interpreted with care.

First, it is not intended to describe the singular initial-time regime, since both the coefficient $\kappa/(2t)$ in the model and the factor $t^{-\kappa/2}$ in the approximation are singular at $t = 0$ whenever $\kappa > 0$. For that reason, the approximation is used only on intervals of the form $[t_{\min}, T]$ with $t_{\min} > 0$.

Second, (20) is a formal predictor rather than an exact solution. Indeed, the Caputo derivative does not satisfy a simple classical product rule, and the nonlinear term $\mu\, u u_x$

introduces higher-order couplings between the amplitude $A(t)$ and the reference profile U. Consequently, the role of (20) is not to provide an exact representation of the full model, but to supply a physically meaningful leading-order approximation whose consistency can be assessed through residual diagnostics.

Third, the classical limit is recovered in a natural way. As $\alpha \to 1$,

$$E_\alpha(-\delta t^\alpha) \to e^{-\delta t}, \qquad \frac{t^\alpha}{\Gamma(1+\alpha)} \to t,$$

and therefore (20) formally reduces to

$$u_{\text{app}}(x,t) \approx t^{-\kappa/2} e^{-\delta t}\, U(x,t), \qquad t \geq t_{\min} > 0. \tag{21}$$

This is consistent with the expected combination of exponential damping and nonplanar attenuation in the classical setting.

4.5. Examples Based on Classical KdV Waves

If U is the classical one-soliton solution

$$U(x,\tau) = \frac{2\nu k^2}{\mu}\, \operatorname{sech}^2\!\left(\frac{k}{2}\big(x - \nu k^2 \tau - x_0\big)\right), \tag{22}$$

then (20) yields the approximate fractional profile

$$u_{\text{app}}(x,t) \approx t^{-\kappa/2} E_\alpha(-\delta t^\alpha)\, \frac{2\nu k^2}{\mu}\, \operatorname{sech}^2\!\left[\frac{k}{2}\left(x - \nu k^2 \frac{t^\alpha}{\Gamma(1+\alpha)} - x_0\right)\right], \qquad t \geq t_{\min} > 0. \tag{23}$$

More generally, if U is a classical multi-soliton or periodic KdV solution, then the same modulation principle gives the formal approximation

$$u_{\text{app}}(x,t) \approx t^{-\kappa/2} E_\alpha(-\delta t^\alpha)\, U\!\left(x, \frac{t^\alpha}{\Gamma(1+\alpha)}\right), \qquad t \geq t_{\min} > 0, \tag{24}$$

which will be used in the sequel as a reference state for the residual analysis.

4.6. Role in the Present Work

The purpose of the construction above is not to claim exact solvability of the full damped nonplanar fractional equation. Its purpose is to generate analytically transparent reference profiles that encode the expected effects of memory, damping, and geometry in a simple closed form. These profiles provide a useful starting point for the numerical study and, more importantly, for the residual diagnostics developed in the subsequent sections.

4.7. Chebyshev Reconstruction of the Caputo Derivative

There is an alternative and conceptually simpler strategy for evaluating the Caputo derivative that avoids explicit history summation. The idea is to approximate the temporal dependence of the solution by a Chebyshev polynomial on a finite interval. Once this approximation is available, the Caputo derivative can be computed analytically term by term. In this way, the nonlocal difficulty of the fractional operator is transferred to a controlled polynomial approximation step.

4.7.1. Chebyshev approximation on a finite interval

Let $g(t)$ be a sufficiently smooth function defined on a finite interval $t \in [a, b]$. We approximate g by a Chebyshev polynomial of degree n, following the standard spectral approximation viewpoint [26, 27],

$$g(t) \approx P_n(t), \tag{25}$$

constructed by interpolation at Chebyshev–Gauss–Lobatto nodes.

Introducing the reference variable

$$\xi \in [-1, 1], \qquad t = \frac{a+b}{2} + \frac{b-a}{2}\,\xi,$$

the Chebyshev nodes in the reference interval are

$$\xi_k = \cos\left(\frac{\pi k}{n}\right), \qquad k = 0, 1, \ldots, n, \tag{26}$$

which map to the physical nodes

$$t_k = \frac{a+b}{2} + \frac{b-a}{2}\,\xi_k. \tag{27}$$

The function g is sampled at these nodes, and the corresponding Chebyshev coefficients are computed by the usual discrete cosine representation:

$$c_k = \frac{2}{n}\sum_{j=0}^{n} g(t_j)\cos\left(\frac{k\pi j}{n}\right), \qquad k = 0, \ldots, n, \tag{28}$$

with the standard normalization adjustment for the first coefficient.

The resulting approximation takes the form

$$P_n(t) = \sum_{k=0}^{n} c_k\, T_k\left(\frac{2t - (a+b)}{b-a}\right), \tag{29}$$

where T_k denotes the Chebyshev polynomial of the first kind.

4.7.2. Why this simplifies the Caputo derivative

The Caputo derivative is difficult to evaluate numerically because it involves a history integral with a weakly singular kernel. By contrast, the Caputo derivative of a polynomial is known explicitly. For $0 < \alpha < 1$ and integer $m \geq 1$,

$$ {}^{C}D_t^{\alpha} t^m = \frac{\Gamma(m+1)}{\Gamma(m+1-\alpha)}\, t^{m-\alpha}, \qquad {}^{C}D_t^{\alpha} 1 = 0. \tag{30}$$

Since each Chebyshev polynomial $T_k(\xi)$ is a polynomial in ξ, and ξ depends affinely on t, the approximation $P_n(t)$ is ultimately a polynomial in t. Consequently, the Caputo derivative of $P_n(t)$ can be computed exactly by applying (30) term by term.

In practice, the procedure is:

(i) Approximate $g(t)$ on $[a, b]$ by the Chebyshev polynomial $P_n(t)$.

(ii) Rewrite $P_n(t)$ as a polynomial in t.

(iii) Apply the Caputo derivative analytically to each monomial.

Thus no direct history quadrature is required once the polynomial approximation has been constructed.

4.7.3. Application to residual evaluation

In the present work, the Chebyshev reconstruction is applied to the temporal dependence of a candidate solution $U(x, t)$ at fixed spatial locations x. For each such x, the map $t \mapsto U(x, t)$ is approximated on a finite time window by a polynomial of the form

$$U(x, t) \approx P_n^{(x)}(t).$$

The Caputo derivative ${}^{C}D_t^{\alpha} U(x, t)$ is then obtained by differentiating $P_n^{(x)}(t)$ analytically. This expression is substituted into the fractional KdV operator in order to compute the residual.

In this way, the evaluation of the Caputo derivative is transformed from a history-dependent operation into an algebraic one once the Chebyshev coefficients are known.

4.7.4. Accuracy and convergence

For smooth temporal dependence, Chebyshev interpolation converges spectrally, meaning that the approximation error decays rapidly with the polynomial degree n. Therefore, the dominant error in the reconstructed Caputo derivative comes from the polynomial approximation itself rather than from the fractional differentiation step. By increasing n, one may evaluate the Caputo derivative with very high accuracy on the chosen finite time interval.

This makes the Chebyshev approach especially attractive for residual diagnostics, where one seeks high temporal accuracy on a prescribed time window rather than long-time time-marching.

4.7.5. Interpretation and scope

Conceptually, the Chebyshev approach replaces explicit temporal memory by a global temporal representation. Instead of accumulating the past through a history sum, the temporal history is encoded in the polynomial coefficients. Once this encoding is available, the Caputo derivative becomes an explicit algebraic operation.

The method is not intended for strongly nonsmooth temporal behavior or for very long time intervals. Its natural range of applicability is the diagnostic evaluation of fractional operators on moderate time windows, which is precisely the setting considered in the present work. In this sense, the Chebyshev reconstruction provides a useful complement to history-based discretizations such as L1 and the strong finite-difference approximation.

5. Numerical Experiments and Discussion

In this section we present representative numerical experiments illustrating the behavior of the formal approximate profiles introduced in Section 4, together with the associated residual diagnostics for the damped nonplanar time–fractional Korteweg–de Vries equation

$$ {}^{C}D_t^{\alpha} u + \mu\, u u_x + \nu\, u_{xxx} + \left(\frac{\kappa}{2t} + \delta\right) u = 0, \qquad 0 < \alpha < 1. \tag{31} $$

The computations are carried out on truncated time intervals

$$ t \in [t_{\min}, T], \qquad t_{\min} > 0, \tag{32} $$

since, for $\kappa > 0$, both the coefficient $\kappa/(2t)$ in the model and the attenuation factor $t^{-\kappa/2}$ in the analytical approximant are singular at $t = 0$.

The purpose of this section is not to claim exact solvability of the full fractional model, but rather to quantify the consistency of the proposed approximation framework through explicit residual evaluation. Throughout the computations, the Caputo derivative is approximated by the graded-mesh L1 discretization introduced in Section 3, which is particularly suitable for resolving the weakly singular early-time regime. In this way, the numerical experiments provide a direct test of how well the modulated KdV profiles reproduce the behavior of the full fractional operator.

5.1. Common Diagnostic Quantities

For a given approximate profile $u_{\mathrm{app}}(x,t)$, we define the residual associated with (31) by

$$ R(x,t) = {}^{C}D_t^{\alpha} u_{\mathrm{app}}(x,t) + \mu\, u_{\mathrm{app}}(x,t)\, \partial_x u_{\mathrm{app}}(x,t) + \nu\, \partial_x^3 u_{\mathrm{app}}(x,t) + \left(\frac{\kappa}{2t} + \delta\right) u_{\mathrm{app}}(x,t). \tag{33} $$

At selected times $t = t_\ell$, we monitor the spatial norms

$$ \|R(\cdot,t_\ell)\|_{L^2} = \left(\int_{x_{\min}}^{x_{\max}} |R(x,t_\ell)|^2\, dx\right)^{1/2}, \qquad \|R(\cdot,t_\ell)\|_{L^\infty} = \max_{x\in[x_{\min},x_{\max}]} |R(x,t_\ell)|. \tag{34} $$

Unless otherwise stated, each numerical example is discussed according to the same general structure:

(i) the time evolution of the residual norms,

(ii) the spatial structure of the residual at representative times,

(iii) a three–dimensional visualization of the approximate solution, and

(iv) the interpretation of the observed residual behavior in terms of fractional memory, damping, and nonplanar attenuation.

5.2. General Remarks

Before turning to the individual examples, it is useful to record several observations that recur throughout this section.

- Residual peaks are typically associated with the early-time regime, where fractional memory and nonautonomous attenuation interact most strongly.
- The damping coefficient δ contributes a Mittag–Leffler-type attenuation that generally reduces the residual as time increases.
- The nonplanar parameter κ strengthens the initial mismatch through the explicitly singular factor $\kappa/(2t)$, making the interval near $t = 0$ the most delicate part of the evolution.
- Even when the residual is not negligible, its structure remains spatially coherent and therefore provides useful information about the range of validity of the analytical approximant.

These general features are illustrated concretely in the examples below.

5.3. Example 1: Planar Single-Soliton Benchmark

Problem setup. As a first benchmark, we consider the planar undamped case

$$\kappa = 0, \qquad \delta = 0,$$

for which the damped nonplanar time-fractional Korteweg–de Vries equation reduces to

$$ {}^{C}D_t^{\alpha} u + \mu\, u u_x + \nu\, u_{xxx} = 0, \qquad 0 < \alpha < 1. \tag{35}$$

This example is intended to isolate the effect of fractional memory without the additional influence of geometric attenuation or linear damping.

We take as reference the classical one-soliton KdV profile and apply the fractional time deformation described in Section 4. In the normalized case $\mu = 6$, $\nu = 1$, with

$$k = 0.2, \qquad \alpha = 0.9,$$

the approximate profile becomes

$$u_{\mathrm{app}}(x,t) = \frac{k^2}{3}\,\mathrm{sech}^2\!\left(\frac{k}{2}\left(x - \frac{k^2 t^{\alpha}}{\Gamma(1+\alpha)}\right)\right), \qquad t \in [t_{\min}, T]. \tag{36}$$

For the present computation we use

$$-30 \le x \le 30, \qquad 0.1 \le t \le 2, \qquad h = 0.1.$$

Residual evaluation. The residual associated with (35) is

$$R(x,t) = {}^{C}D_t^{\alpha} u_{\mathrm{app}}(x,t) + 6\,u_{\mathrm{app}}(x,t)\,\partial_x u_{\mathrm{app}}(x,t) + \partial_x^3 u_{\mathrm{app}}(x,t). \tag{37}$$

The Caputo derivative is evaluated numerically using the graded-mesh L1 scheme introduced in Section 3, with grading exponent $\gamma = 2$.

Global residual error. The computed global maximum of the residual on the computational window is

$$\max_{\substack{-30\le x\le 30\\ 0.1\le t\le 2}} |R(x,t)| \approx 3.40162 \times 10^{-5}, \tag{38}$$

attained at approximately

$$x \approx 4.93997, \qquad t = 0.1.$$

This shows that the largest mismatch occurs at the earliest time considered, which is consistent with the stronger influence of fractional memory near the initial stage of the evolution.

Residual error at selected times. To quantify the temporal behavior more explicitly, we computed the maximum residual over space at several representative times. The resulting values are listed in Table 2.

Comments on Table 2. Several features are worth emphasizing.

First, the residual remains uniformly small throughout the whole computational interval, staying at the level of 10^{-5}. This indicates that the approximate profile (36) is internally consistent with the fractional model in the planar undamped regime.

Second, the residual decreases monotonically from 3.40162×10^{-5} at $t = 0.1$ to 3.06001×10^{-5} at $t = 2$. Although the decay is mild, it is systematic. This suggests that the strongest discrepancy is concentrated in the early-time regime, where the fractional memory term is most sensitive to the initial deformation of the classical KdV soliton.

Third, because $\kappa = 0$ and $\delta = 0$, the observed residual comes solely from the mismatch between the classical traveling-wave template and the fractional time evolution. In other words, this benchmark isolates the pure effect of the Caputo time deformation.

Table 2: Example 1. Maximum residual error over space at selected times.

t	$\max_x \lvert R(x,t)\rvert$
0.10	3.40162×10^{-5}
0.29	3.15636×10^{-5}
0.48	3.10838×10^{-5}
0.67	3.08903×10^{-5}
0.86	3.07876×10^{-5}
1.05	3.07247×10^{-5}
1.24	3.06825×10^{-5}
1.43	3.06526×10^{-5}
1.62	3.06304×10^{-5}
1.81	3.06134×10^{-5}
2.00	3.06001×10^{-5}

Residual profiles at several times. Figure 1 shows the spatial distribution of $|R(x,t)|$ for several representative times. The profiles are symmetric with respect to the origin and display two dominant lobes away from the center. In contrast, the residual is very small near the midpoint $x = 0$. This indicates that the mismatch is not concentrated at the crest center itself, but rather in the regions where the profile changes most rapidly.

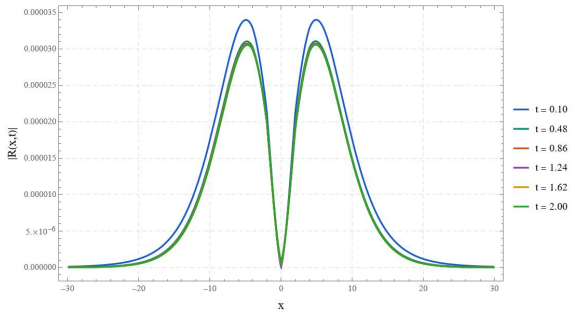

Figure 1: Example 1. Spatial profiles of the absolute residual $|R(x,t)|$ at several representative times. The curves remain close to each other and exhibit a slow decrease in amplitude as time increases.

Approximate solution surface. The approximate solution surface is shown in Figure 2. The profile preserves the expected localized KdV shape while evolving according to the fractional time deformation. Since no damping and no nonplanar attenuation are included in this benchmark, the amplitude remains essentially controlled by the deformation of the propagation law rather than by an additional decay factor.

Residual surface. Figure 3 presents the spatiotemporal residual surface. The dominant feature is a pair of smooth ridges that persist throughout the time interval while slowly decreasing in height. No abrupt spikes or irregular oscillations are observed, which supports the numerical stability of the graded-mesh L1 evaluation used in this example.

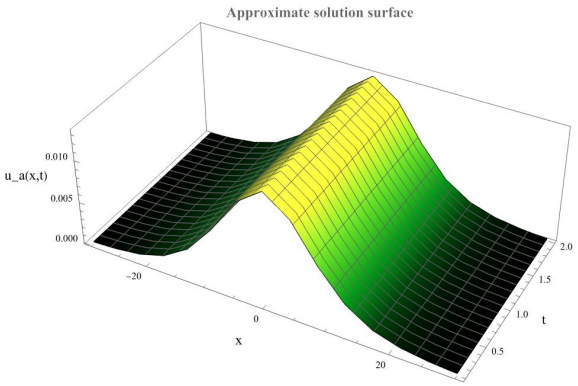

Figure 2: Example 1. Approximate solution surface $u_{\mathrm{app}}(x,t)$ for the planar undamped fractional benchmark.

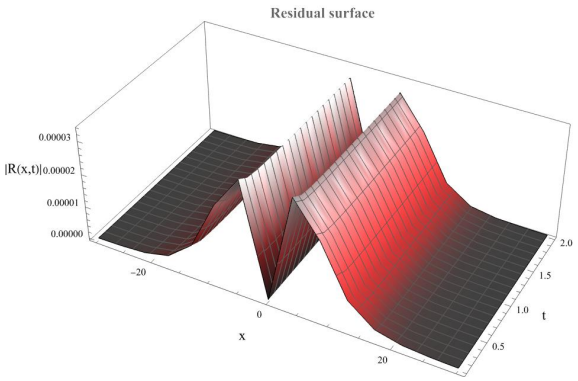

Figure 3: Example 1. Spatiotemporal surface of the absolute residual $|R(x,t)|$. The strongest mismatch occurs near the earliest time and then decreases gradually.

Time evolution of the maximum residual. The monotone temporal trend is shown more clearly in Figure 4, where we plot

$$t \mapsto \max_{x} |R(x,t)|.$$

The curve confirms that the maximum residual is attained at the beginning of the computational interval and then decreases steadily.

Interpretation. This first benchmark provides a useful baseline for the entire study. Because no damping or geometric spreading is present, the residual reflects only the discrepancy introduced by replacing the classical time variable with its fractional counterpart. The fact that the residual remains small and decreases mildly in time shows that the modulated one-soliton profile is a meaningful approximate solution in the planar case.

At the same time, the residual is not zero, which is important: this confirms that the fractional profile is not an exact solution of the full time-fractional equation. Therefore, Example 1 supports the central viewpoint of the paper, namely that the proposed profiles should be interpreted as analytically transparent leading-order approximations whose validity must be assessed through explicit residual diagnostics rather than assumed a priori.

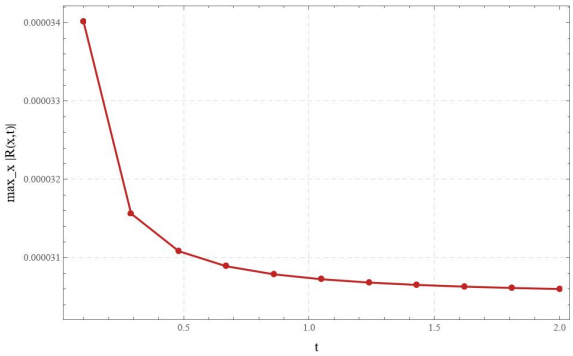

Figure 4: Example 1. Time evolution of the spatial maximum of the residual. The gradual decay indicates that the approximation becomes slightly more consistent as time increases over the interval considered.

5.4. Example 2: Planar Damped Single-Soliton Benchmark

Problem setup. As a second benchmark, we consider the planar damped case

$$\kappa = 0, \qquad \delta > 0,$$

for which the damped nonplanar time-fractional Korteweg–de Vries equation reduces to

$$^{C}D_t^{\alpha} u + \mu\, u u_x + \nu\, u_{xxx} + \delta u = 0, \qquad 0 < \alpha < 1. \tag{39}$$

This example is intended to isolate the combined influence of fractional memory and linear damping, without the additional effect of nonplanar geometric attenuation.

In the present computation we take

$$\mu = 6, \qquad \nu = 1, \qquad k = 0.1, \qquad \alpha = 0.9, \qquad \delta = 0.2,$$

on the computational domain

$$-50 \le x \le 50, \qquad 0.1 \le t \le 5,$$

with time step $h = 0.1$.

Analytical approximant. Starting from the classical one-soliton KdV profile and introducing both the fractional time deformation and the Mittag–Leffler damping factor, we use the analytical approximant

$$u_{\mathrm{app}}(x,t) = E_{\alpha}(-\delta t^{\alpha})\, \frac{k^2}{3}\, \operatorname{sech}^2\!\left(\frac{k}{2}\left(x - \frac{k^2 t^{\alpha}}{\Gamma(1+\alpha)}\right)\right). \tag{40}$$

For the parameter values used here, this becomes

$$u_{\mathrm{app}}(x,t) = \frac{1}{300}\, E_{0.9}(-0.2\, t^{0.9})\, \operatorname{sech}^2\!\left(0.05\left(x - \frac{0.01\, t^{0.9}}{\Gamma(1.9)}\right)\right). \tag{41}$$

Residual evaluation. The residual associated with (39) is

$$R(x,t) = {}^{C}D_t^{\alpha} u_{\mathrm{app}}(x,t) + 6\, u_{\mathrm{app}}(x,t)\, \partial_x u_{\mathrm{app}}(x,t) + \partial_x^3 u_{\mathrm{app}}(x,t) + \delta\, u_{\mathrm{app}}(x,t). \tag{42}$$

The Caputo derivative is evaluated numerically by means of the graded-mesh L1 approximation introduced in Section 3.

Global residual error. The computed global maximum of the residual on the computational window is

$$\max_{\substack{-50\le x\le 50\\ 0.1\le t\le 5}} |R(x,t)| \approx 6.87766 \times 10^{-5}, \tag{43}$$

attained approximately at

$$x \approx -0.502676, \qquad t = 0.1.$$

Thus the largest mismatch occurs at the earliest time considered, which is consistent with the stronger influence of fractional memory near the beginning of the evolution.

Residual error at selected times. To examine the temporal behavior more explicitly, we computed the maximum residual over space at several representative times. The resulting values are listed in Table 3.

Table 3: Example 2. Maximum residual error over space at selected times.

t	$\max_x \lvert R(x,t)\rvert$
0.10	6.87766×10^{-5}
0.59	1.63611×10^{-5}
1.08	1.08822×10^{-5}
1.57	8.50303×10^{-6}
2.06	7.06977×10^{-6}
2.55	6.07135×10^{-6}
3.04	5.31758×10^{-6}
3.53	4.71940×10^{-6}
4.02	4.22864×10^{-6}
4.51	3.81645×10^{-6}
5.00	3.46424×10^{-6}

Comments on Table 3. Several features are immediate.

First, the residual remains uniformly small throughout the whole computational interval, staying between 10^{-5} and 10^{-6} after the initial stage. This indicates that the damped fractional profile (40) is internally consistent with the planar damped model in the parameter regime considered.

Second, the residual decreases strongly and monotonically in time. In particular, the maximum residual drops from 6.87766×10^{-5} at $t = 0.10$ to 3.46424×10^{-6} at $t = 5.00$,

which corresponds to a reduction of about 95%. This behavior is consistent with the presence of the damping factor $E_\alpha(-\delta t^\alpha)$, which progressively reduces the amplitude of the profile and therefore weakens the mismatch with the governing equation.

Third, the residual level in this benchmark is significantly smaller than the one observed in the nonplanar cases. This is expected, since here the only attenuation mechanism is the Mittag–Leffler damping factor, without the additional explicitly singular geometric term $\kappa/(2t)$.

Residual profiles at several times. Figure 5 shows the spatial distribution of $|R(x,t)|$ for several representative times. The residual is centered near the soliton crest and has a smooth bell-shaped structure. This is natural, since the damping contribution δu_{app} is strongest where the solution itself is largest, namely near the wave center. As time increases, the profiles keep the same qualitative shape but decrease rapidly in amplitude.

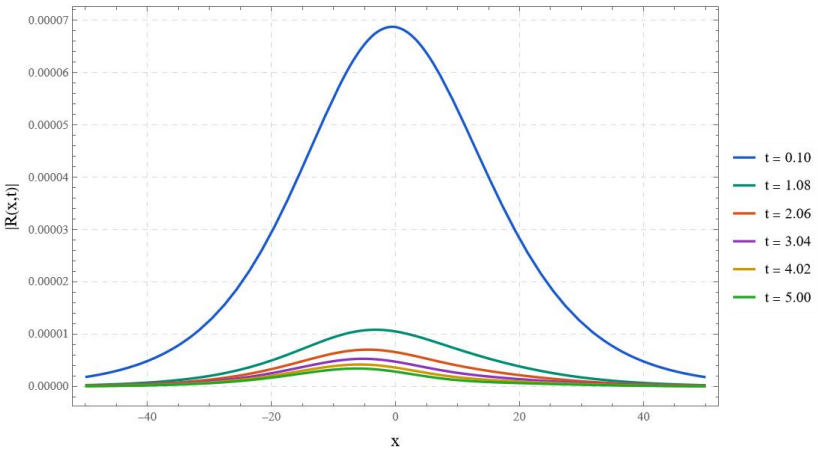

Figure 5: Example 2. Spatial profiles of the absolute residual $|R(x,t)|$ at several representative times. The residual remains centered near the wave crest and decays markedly in amplitude as time increases.

Approximate solution surface. The approximate solution surface is shown in Figure 6. The wave remains localized and smooth throughout the computational window, while its amplitude decreases in time because of the Mittag–Leffler damping factor. Since $\kappa = 0$, this attenuation is entirely due to damping and not to geometric spreading.

Residual surface. Figure 7 presents the corresponding spatiotemporal residual surface. The residual is largest near the initial stage and near the wave crest, then decreases smoothly in both time and amplitude. No oscillatory instability or irregular structure is visible. Instead, the surface is coherent and monotone, which supports the numerical robustness of the graded-mesh L1 discretization in this damped case.

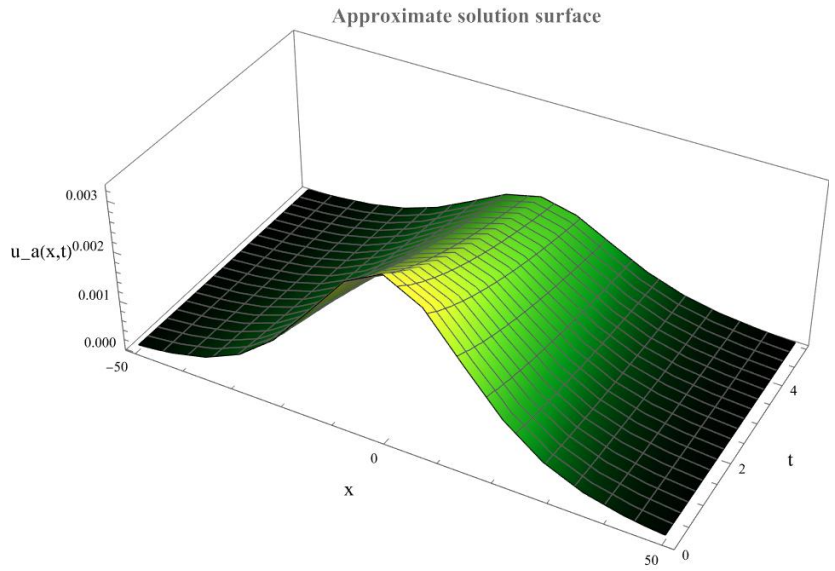

Figure 6: Example 2. Approximate solution surface $u_{\mathrm{app}}(x,t)$ for the planar damped fractional benchmark. The wave remains localized while its amplitude decreases under Mittag–Leffler damping.

Time evolution of the maximum residual. The temporal decay is shown more clearly in Figure 8, where we plot

$$t \mapsto \max_x |R(x,t)|.$$

The curve decreases rapidly at early times and then continues to decay more gradually, confirming that the approximate profile becomes increasingly consistent as the damping suppresses the wave amplitude.

Interpretation. This benchmark confirms that the analytical approximant (40) provides a meaningful leading-order description of the damped fractional dynamics in the planar case. The residual is not zero, so the profile should not be interpreted as an exact solution of the full fractional model. However, the residual remains small, spatially coherent, and strongly decreasing in time.

From a physical viewpoint, Example 2 shows that the addition of linear damping changes the character of the residual relative to the undamped planar benchmark. In the purely undamped case, the mismatch originates mainly from the fractional time deformation of the traveling-wave template. Here, by contrast, the residual is increasingly dominated by a crest-centered amplitude correction induced by the Mittag–Leffler relaxation. Thus the example illustrates clearly how damping and fractional memory interact: the damping term introduces an additional source of mismatch, but it also regularizes the evolution and produces a substantial reduction of the residual as time increases.

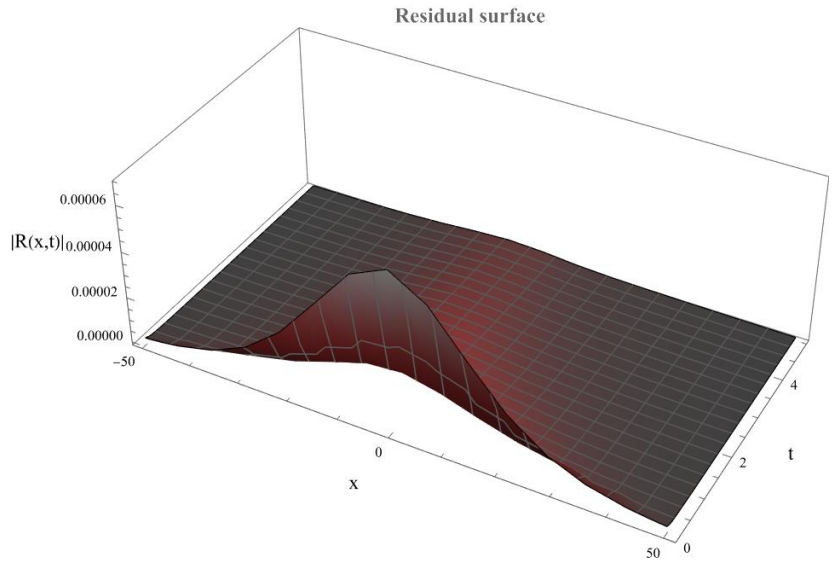

Figure 7: Example 2. Spatiotemporal surface of the absolute residual $|R(x,t)|$. The dominant mismatch is concentrated near the earliest time and then decreases steadily.

5.5. Example 3: Cylindrical Nonplanar Damped Single-Soliton Benchmark

Problem setup. As a third benchmark, we consider the cylindrical nonplanar damped case

$$\kappa = 1, \qquad \delta > 0,$$

for which the damped nonplanar time-fractional Korteweg–de Vries equation becomes

$$^{C}D_t^{\alpha} u + \mu\, u u_x + \nu\, u_{xxx} + \left(\frac{1}{2t} + \delta\right) u = 0, \qquad 0 < \alpha < 1. \tag{44}$$

This example is designed to assess the combined effect of fractional memory, linear damping, and cylindrical geometric attenuation.

In the present computation we take

$$\mu = 6, \qquad \nu = 1, \qquad k = 0.1, \qquad \alpha = 0.9, \qquad \delta = 0.2, \qquad \kappa = 1,$$

on the computational domain

$$-50 \le x \le 50, \qquad 0.1 \le t \le 5,$$

with time step $h = 0.1$.

Analytical approximant. Starting from the classical one-soliton KdV profile and applying both the fractional time deformation and the cylindrical attenuation factor, we use the analytical approximant

$$u_{\mathrm{app}}(x,t) = t^{-1/2} E_{\alpha}(-\delta t^{\alpha}) \frac{k^2}{3} \operatorname{sech}^2\left(\frac{k}{2}\left(x - \frac{k^2 t^{\alpha}}{\Gamma(1+\alpha)}\right)\right), \qquad t \ge t_{\min} > 0. \tag{45}$$

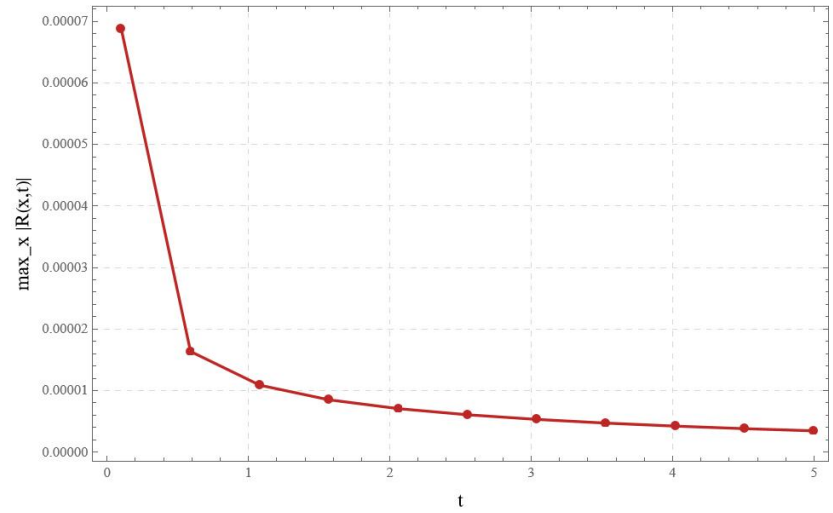

Figure 8: Example 2. Time evolution of the spatial maximum of the residual. The steep initial drop is followed by a slower long-time decay.

For the parameter values used here, this becomes

$$u_{\mathrm{app}}(x,t) = \frac{1}{300\sqrt{t}}\, E_{0.9}(-0.2\, t^{0.9})\, \operatorname{sech}^2\!\left(0.05\left(x - \frac{0.01\, t^{0.9}}{\Gamma(1.9)}\right)\right). \tag{46}$$

Residual evaluation. The residual associated with (44) is

$$R(x,t) = {}^{C}D_t^{\alpha} u_{\mathrm{app}}(x,t) + 6\, u_{\mathrm{app}}(x,t)\, \partial_x u_{\mathrm{app}}(x,t) + \partial_x^3 u_{\mathrm{app}}(x,t) + \left(\frac{1}{2t} + \delta\right) u_{\mathrm{app}}(x,t). \tag{47}$$

The Caputo derivative is again evaluated numerically by the graded-mesh L1 approximation described in Section 3.

Global residual error. A direct maximization of the interpolated residual field on the full computational window gives

$$\max_{\substack{-50\le x\le 50\\ 0.1\le t\le 5}} |R(x,t)| \approx 1.60947 \times 10^{-2}, \tag{48}$$

attained approximately at

$$x \approx -9.4505 \times 10^{-18} \approx 0, \qquad t \approx 0.199044.$$

This indicates that the strongest mismatch is concentrated in a narrow early-time layer around the wave center, where the explicitly singular factor $t^{-1/2}$ and the nonautonomous coefficient $1/(2t)$ are still dominant.

Residual error at selected times. To obtain a more transparent time-resolved picture, we also computed the spatial maximum of the residual at several representative times. The resulting values are listed in Table 4.

Table 4: Example 3. Maximum residual error over space at selected times.

t	$\max_x \lvert R(x,t)\rvert$
0.10	2.51515×10^{-3}
0.59	3.16573×10^{-3}
1.08	1.68753×10^{-3}
1.57	1.19023×10^{-3}
2.06	9.28436×10^{-4}
2.55	7.64321×10^{-4}
3.04	6.51049×10^{-4}
3.53	5.67874×10^{-4}
4.02	5.04078×10^{-4}
4.51	4.53528×10^{-4}
5.00	4.12458×10^{-4}

Comments on Table 4. Several features are worth noting.

First, unlike the purely damped planar case of Example 2, the residual does not decrease monotonically from the first recorded time. Instead, it increases from 2.51515×10^{-3} at $t = 0.10$ to 3.16573×10^{-3} at $t = 0.59$, and only after that does it begin a steady decay. This nonmonotone behavior is a clear signature of the cylindrical geometric factor $t^{-1/2}$, which amplifies the early-time sensitivity of the approximate profile.

Second, after this short transient, the residual decreases systematically. From the sampled peak value 3.16573×10^{-3} at $t = 0.59$ to the final value 4.12458×10^{-4} at $t = 5$, the reduction is approximately 87%. Thus, although the cylindrical attenuation strengthens the initial mismatch, it also leads to a strong progressive reduction of the residual once the solution moves away from the singular initial-time regime.

Third, the error level in this example is substantially larger than in Examples 1 and 2. This is expected. In addition to the fractional memory and the damping term, the approximant now contains the explicitly singular factor $t^{-1/2}$, and the equation itself includes the nonautonomous coefficient $1/(2t)$. Their interaction produces a more demanding consistency test.

Residual profiles at several times. Figure 9 shows the spatial profiles of $|R(x,t)|$ for several representative times. In contrast with the double-lobed structure observed in the undamped planar benchmark, the residual is now strongly centered at the origin and has a bell-shaped form. This is natural: both the solution amplitude and the geometric correction are strongest near the wave crest, so the residual becomes concentrated around the central core.

As time increases, the profiles keep essentially the same shape but their amplitudes decrease markedly. This indicates that the principal effect of the cylindrical factor is not to distort the spatial structure of the residual, but rather to magnify its early-time amplitude.

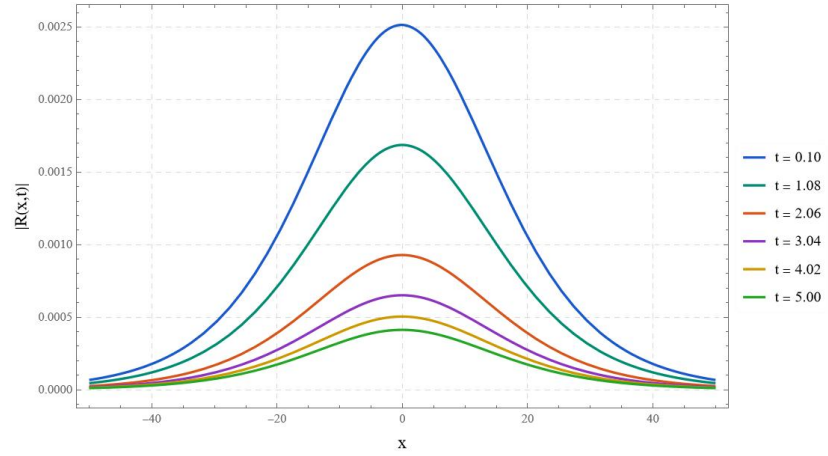

Figure 9: Example 3. Spatial profiles of the absolute residual $|R(x,t)|$ at several representative times. The residual is concentrated near the wave crest and exhibits a pronounced early-time amplification before decaying.

Approximate solution surface. The approximate solution surface is shown in Figure 10. Compared with the planar damped case, the amplitude now decreases more rapidly near the initial stage because of the extra factor $t^{-1/2}$. Nevertheless, the profile remains localized and smooth throughout the computational window. The resulting wave is therefore still coherent, but it is attenuated more strongly than in Example 2.

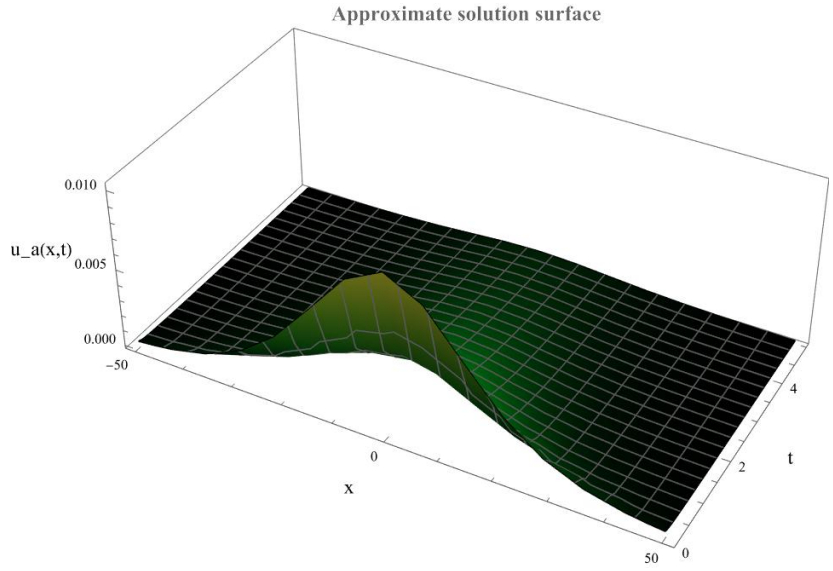

Figure 10: Example 3. Approximate solution surface $u_{\mathrm{app}}(x,t)$ in the cylindrical nonplanar damped case. The localization is preserved, while the amplitude is more strongly reduced at early times by the factor $t^{-1/2}$.

Residual surface. Figure 11 presents the spatiotemporal residual surface. The strongest part of the residual is concentrated near the wave center and in the early-time region. After the transient, the surface decreases smoothly in height, in agreement with the values

reported in Table 4. No irregular oscillations are visible, which supports the numerical stability of the graded-mesh evaluation even in the presence of the explicitly singular geometric factor.

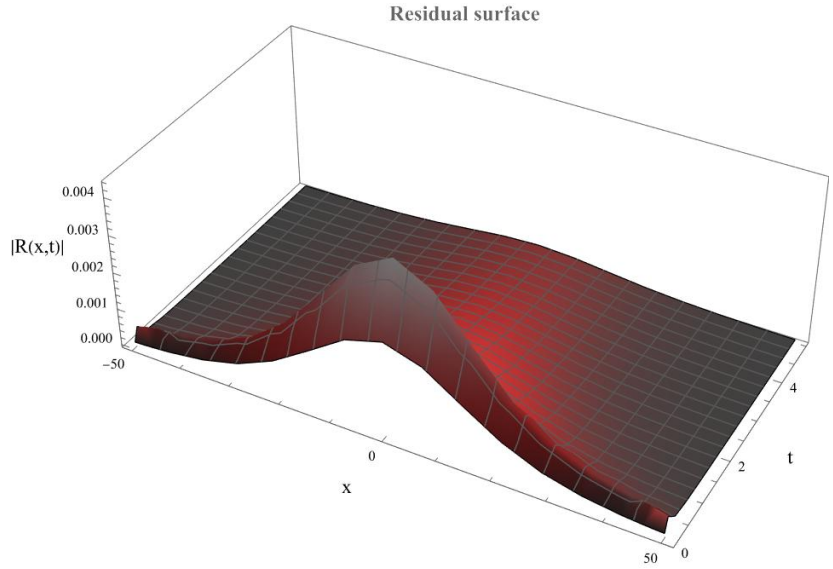

Figure 11: Example 3. Spatiotemporal surface of the absolute residual $|R(x,t)|$. The main contribution is concentrated near the crest and within the early-time transient region.

Time evolution of the maximum residual. The temporal behavior of the spatial maximum is displayed in Figure 12. The curve highlights the short early-time increase followed by a long monotone decay. This behavior is qualitatively different from Example 2 and confirms that the cylindrical geometric term changes the character of the residual dynamics.

Interpretation. This benchmark clarifies the role of cylindrical nonplanar attenuation in the fractional KdV framework. The analytical approximant (45) remains a meaningful leading-order description of the solution, but the residual is clearly larger than in the planar cases. This is not a defect of the computation; rather, it reflects the stronger consistency demands imposed by the explicitly time-singular factor $t^{-1/2}$ and the nonautonomous coefficient $1/(2t)$.

From a physical viewpoint, Example 3 shows that cylindrical geometry does not destroy the localized-wave structure, but it substantially amplifies the early-time discrepancy between the modulated classical profile and the full fractional model. Once the solution moves away from the most singular initial regime, the residual decreases steadily, indicating that the approximation becomes progressively more reliable on moderate and larger times.

In this sense, Example 3 is especially important for the paper: it demonstrates that the proposed approximation framework can still be used in genuinely nonplanar fractional set-

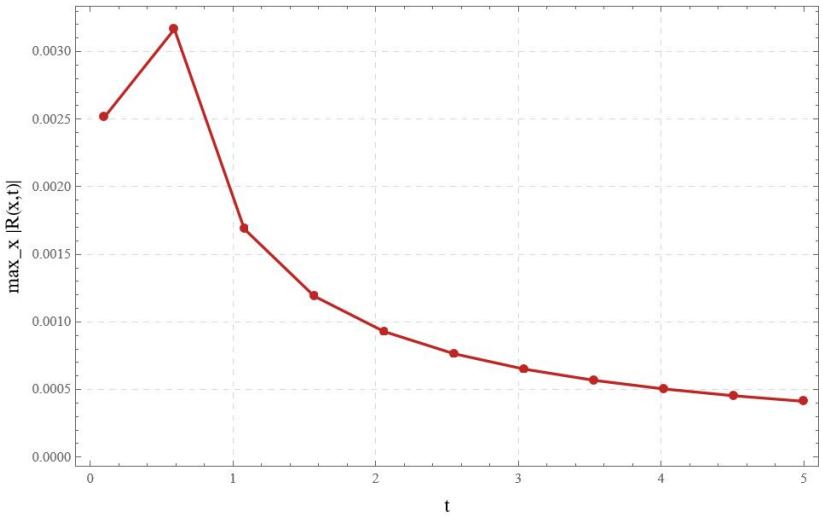

Figure 12: Example 3. Time evolution of the spatial maximum of the residual. A short initial growth is followed by a sustained decay as the influence of the cylindrical singular factor weakens.

tings, but only with the explicit understanding that the strongest mismatch is concentrated near early times and must be quantified rather than ignored.

Taken together, the numerical experiments show that the proposed approximation framework captures the dominant wave behavior of the damped nonplanar fractional KdV model while making clear where its limitations lie. In the planar cases, the residuals remain small and typically decrease in time, indicating that the modulated classical profiles provide meaningful leading-order descriptions of the fractional dynamics. In the nonplanar cases, the residuals are stronger near the initial regime because of the explicitly singular geometric coefficient, but they still become progressively more controlled on later time intervals. These observations confirm that the analytical profiles should not be interpreted as exact fractional solutions, but rather as reference states whose validity is time-dependent and parameter-dependent. This residual-based viewpoint provides the natural bridge to the broader interpretation and conclusions developed in the next section.

6. Analysis and Discussion

The numerical experiments reported above provide a residual-based assessment of the proposed approximation strategy for the damped nonplanar time-fractional Korteweg–de Vries equation. Rather than treating the analytical profiles as exact solutions of the fractional model, the computations were designed to quantify their consistency through the residual generated by the full operator. This viewpoint is essential in the present setting, because the profiles are obtained by modulating known classical KdV solutions through a fractional time deformation and an attenuation law, and therefore must be interpreted as formal leading-order predictors rather than exact closed-form solutions.

A first general conclusion is that the residual diagnostics remain bounded and structurally coherent in all benchmark regimes considered. This is important because it shows

that the proposed approximation framework preserves the dominant wave morphology of the underlying classical KdV templates even after fractional memory, damping, and geometric attenuation are introduced. In particular, the computed solution surfaces retain the expected localized-wave structure, while the residuals remain concentrated in physically meaningful regions, typically near the wave crest and, when $\kappa > 0$, near the early-time regime where the nonautonomous geometric coefficient is strongest.

The planar undamped benchmark provides the cleanest baseline for interpretation. In that case, the residual is generated solely by the mismatch between the classical traveling-wave profile and the fractional time evolution. The fact that the residual remains small and decreases mildly in time indicates that the fractional time deformation alone already provides a meaningful first approximation of the dynamics. Thus the planar undamped case confirms that the residual framework is capable of isolating the pure contribution of Caputo memory without contamination from damping or geometric effects.

The planar damped benchmark clarifies the role of Mittag–Leffler attenuation. In that regime, the residual becomes strongly centered around the wave crest and decreases markedly in time. This behavior is natural, since the damping correction acts directly on the solution amplitude and is therefore strongest where the profile itself is largest. From the numerical results, one sees that damping plays a dual role: it introduces an additional source of discrepancy at early times, but it also regularizes the subsequent evolution and leads to a systematic reduction of the residual as time increases. In this sense, damping improves the long-time consistency of the approximate profile, even though it does not eliminate the initial mismatch created by fractional memory.

The genuinely nonplanar benchmark reveals the specific influence of geometric attenuation. Once the factor $\kappa/(2t)$ is turned on, the residual becomes substantially larger in the early-time regime and develops a more pronounced transient character. This is precisely what should be expected from the structure of the model: for $\kappa > 0$, both the equation and the approximate profile contain explicitly singular time-dependent factors, so the interval near $t = 0$ is necessarily the most delicate one. At the same time, the numerical experiments show that this stronger early-time mismatch does not destroy the validity of the approximation on moderate time intervals. After the initial transient, the residual decreases steadily, indicating that the approximation becomes progressively more reliable once the influence of the singular geometric coefficient weakens.

From a broader perspective, the numerical experiments demonstrate that the main source of residual growth is not spatial complexity alone but temporal nonlocality. Fractional memory reacts most strongly when the profile experiences rapid effective temporal change, and this effect is amplified further when damping or nonplanar attenuation is present. For this reason, the most informative part of the residual analysis is the early-time regime, where the competition between the Caputo memory term, the attenuation law, and the transported KdV profile is strongest. The graded-mesh L1 discretization adopted in this work is therefore particularly appropriate, since it was designed precisely to resolve this weakly singular region more accurately than a uniform-grid discretization.

Another important conclusion is methodological. The results support the idea that residual diagnostics provide a more honest and transparent framework than simply pre-

senting deformed classical profiles as if they were fractional solutions. The analytical expressions used here do reproduce the main qualitative behavior of the waves, but the residual calculations reveal where this approximation is strongest and where it is weakest. In the planar cases, the mismatch remains relatively small and decreases in time; in the nonplanar regime, the mismatch is stronger near the initial time but still becomes controlled on later intervals. This kind of information would be invisible without an explicit residual analysis.

Overall, the experiments support a consistent interpretation of the proposed framework: the modulated KdV profiles are not exact solutions of the full fractional equation, but they do capture its dominant wave behavior in a quantitatively meaningful way over finite time windows. Their validity is best understood not as an all-or-nothing property, but as a time-dependent and parameter-dependent approximation quality that can be measured directly through the residual.

7. Conclusions

In this work we studied a damped nonplanar time-fractional Korteweg–de Vries equation with Caputo time derivative, combining nonlinear convection, dispersion, linear damping, and nonautonomous geometric attenuation in a single wave model. The purpose of the analysis was not to claim exact solvability of the full fractional equation, but rather to construct analytically transparent approximate profiles and to assess their consistency by direct residual diagnostics.

The starting point of the construction was a family of known classical KdV solutions, used as reference wave templates. By combining a fractional time deformation with a leading-order attenuation factor involving both Mittag–Leffler damping and the nonplanar coefficient, we obtained explicit approximate localized-wave profiles. These expressions preserve a clear connection with the classical integer-order KdV theory while incorporating the main qualitative effects expected from fractional temporal memory and nonautonomous attenuation.

A central contribution of the paper is the residual-based viewpoint adopted throughout. Instead of assuming that the deformed classical profiles remain valid after fractionalization, we tested them directly against the full damped nonplanar operator. This yielded a transparent quantitative measure of consistency and made it possible to determine where the approximation is reliable and where the mismatch is strongest. In particular, the computations showed that the dominant residual contribution is concentrated near the early-time regime, especially when the nonplanar coefficient is present, whereas the approximation becomes progressively more consistent at later times.

The numerical results also clarified the distinct roles of the main parameters. The fractional order controls the temporal deformation of the propagation law and therefore influences the persistence of the wave. The damping coefficient introduces Mittag–Leffler attenuation and tends to reduce the residual over time by suppressing the wave amplitude. The nonplanar parameter produces the strongest early-time correction through the explicitly singular geometric factor, making the initial regime the most delicate part of

the dynamics. Taken together, these effects confirm that the analytical profiles used in the paper should be interpreted as leading-order approximations whose validity depends explicitly on time and on the model parameters.

From a numerical perspective, the graded-mesh L1 discretization proved well suited to the residual evaluation problem considered here. Because the main difficulty lies near the initial time, where weak singular behavior is expected, the graded mesh provides a stable and practical way to approximate the Caputo derivative without introducing unnecessary complexity. The auxiliary Chebyshev reconstruction, while not used as the principal discretization, offers an additional diagnostic viewpoint on moderate time intervals and supports the same general interpretation of the approximation framework.

The overall conclusion is therefore twofold. On the one hand, classical KdV wave forms remain useful and physically meaningful reference states in the time-fractional damped and nonplanar setting. On the other hand, their validity cannot be assumed and must be checked explicitly at the operator level. The present work shows that residual diagnostics provide a natural and effective way to carry out that verification. In this sense, the paper reframes the study of fractional KdV-type equations from a search for exact formulas to a controlled analysis of approximate wave structures whose consistency can be quantified directly.

8. Future Work and Perspectives

Several natural directions follow from the present study.

A first extension concerns additional nonplanar regimes and broader wave families. The approach developed here can be applied not only to the planar and cylindrical configurations considered in detail, but also to stronger geometric attenuation and to other classical KdV wave forms, including multi-soliton profiles and periodic traveling waves. Such extensions would help clarify how residual growth depends on the complexity of the reference wave and on the strength of the nonautonomous attenuation.

A second direction concerns related nonlinear dispersive equations. Since the construction is based on using known integer-order solutions as reference states, the same residual-based philosophy can be transferred to modified KdV, Gardner, Kawahara, and other higher-order or mixed-nonlinearity models. This would make it possible to study whether the balance between fractional memory, damping, and geometric spreading observed here persists in broader classes of dispersive wave equations.

A third direction is computational. Although the graded-mesh L1 scheme performs well for the finite time windows considered in this paper, longer simulations and more complicated wave interactions will require improved strategies for handling the memory term efficiently. Fast convolution methods, adaptive temporal grading, and hybrid local-global residual diagnostics may all be useful in that context.

Finally, the present work suggests a broader conceptual program. Instead of viewing fractional nonlinear evolution equations primarily through the lens of exact solution construction, one may regard them as operator-level perturbations of well-understood classical wave models and ask how long, and in what regimes, those classical structures remain

meaningful. Residual diagnostics provide a systematic way to answer that question. From this viewpoint, the methodology developed here should be seen as a first step toward a more general and verifiable theory of fractional dispersive wave approximations.

Acknowledgements

The author thanks the editorial office and reviewers for constructive comments that helped improve the clarity and scope of this work.

References

[1] D. J. Korteweg and G. de Vries. On the change of form of long waves advancing in a rectangular canal. *Philosophical Magazine*, 39:422–443, 1895.

[2] P. D. Lax. Integrals of nonlinear equations of evolution and solitary waves. *Communications on Pure and Applied Mathematics*, 21:467–490, 1968.

[3] M. J. Ablowitz and H. Segur. *Solitons and the Inverse Scattering Transform*. SIAM, Philadelphia, 1981.

[4] R. Hirota. Exact solution of the korteweg–de vries equation for multiple collisions of solitons. *Physical Review Letters*, 27:1192–1194, 1971.

[5] R. Grimshaw. Forced korteweg–de vries equation. *Studies in Applied Mathematics*, 65:159–188, 1981.

[6] T. Kakutani and N. Yamasaki. Soliton solutions of the korteweg–de vries equation with damping. *Journal of the Physical Society of Japan*, 45:674–680, 1978.

[7] M. Caputo. Linear models of dissipation whose q is almost frequency independent. *Geophysical Journal International*, 13:529–539, 1967.

[8] I. Podlubny. *Fractional Differential Equations*. Academic Press, San Diego, 1999.

[9] F. Mainardi. *Fractional Calculus and Waves in Linear Viscoelasticity*. Imperial College Press, London, 2010.

[10] R. Gorenflo, A. A. Kilbas, F. Mainardi, and S. Rogosin. *Mittag–Leffler Functions, Related Topics and Applications*. Springer, Berlin, 2014.

[11] A. A. Golmankhaneh and A. K. Golmankhaneh. Time-fractional korteweg–de vries equation and its soliton solutions. *Applied Mathematics and Computation*, 190:1276–1281, 2007.

[12] Z. Yan. Fractional nonlinear wave equations and their soliton-like solutions. *Journal of Physics A*, 41:355206, 2008.

[13] Z. Li and F. Zeng. Numerical methods for fractional kdv-type equations. *Computers and Mathematics with Applications*, 70:183–198, 2015.

[14] E. A. Az-Zo'bi, A. S. Hussain, M. Iqbal, A. Aljohani, M. A. Tashtoush, N. E. Alsubaie, F. K. A. Al-Hamarneh, N. M. Nazar, and D. Baleanu. Analytical and numerical solutions of mabc fractional advection dispersion models by utilizing the modified physics informed neural networks with impacts of fractional derivative. *Scientific Reports*, 15:43366, 2025.

[15] E. A. Az-Zo'bi et al. Chaotic, bifurcation, sensitivity, modulation stability analysis, and optical soliton structure to the nonlinear coupled konno–oono system in magnetic field. *AIP Advances*, 15:095103, 2025.

[16] M. A. Al Zubi, K. Afef, and E. A. Az-Zo'bi. Assorted spatial optical dynamics of a generalized fractional quadruple nematic liquid crystal system in non-local media. *Symmetry*, 16(6):778, 2024.

[17] E. A. Az-Zo'bi, Q. M. M. Alomari, K. Afef, and M. Inc. Dynamics of generalized time-fractional viscous-capillarity compressible fluid model. *Optical and Quantum Electronics*, 56:629, 2024.

[18] E. Az-Zo'bi, A. F. Al-Maaitah, M. A. Tashtoush, and M. S. Osman. New generalised cubic–quintic–septic nlse and its optical solitons. *Pramana – Journal of Physics*, 96:184, 2022.

[19] E. A. Az-Zo'bi. New kink solutions for the van der waals p-system. *Mathematical Methods in the Applied Sciences*, 42(18):6216–6226, 2019.

[20] F. Mainardi and R. Gorenflo. On mittag–leffler-type functions in fractional evolution processes. *Journal of Computational and Applied Mathematics*, 118:283–299, 2000.

[21] R. Garrappa. Numerical evaluation of two- and three-parameter mittag–leffler functions. *SIAM Journal on Numerical Analysis*, 53:1350–1369, 2015.

[22] A. A. Kilbas, H. M. Srivastava, and J. J. Trujillo. *Theory and Applications of Fractional Differential Equations*. Elsevier, Amsterdam, 2006.

[23] C. Lubich. Discretized fractional calculus. *SIAM Journal on Mathematical Analysis*, 17:704–719, 1986.

[24] Y. Lin and C. Xu. Finite difference/spectral approximations for the time-fractional diffusion equation. *Journal of Computational Physics*, 225:1533–1552, 2007.

[25] F. Zeng, C. Li, F. Liu, and I. Turner. The use of finite difference and finite element approaches for fractional diffusion equations. *Journal of Computational Physics*, 235:45–59, 2013.

[26] L. N. Trefethen. *Spectral Methods in MATLAB*. SIAM, Philadelphia, 2000.

[27] J. P. Boyd. *Chebyshev and Fourier Spectral Methods*. Dover, New York, 2001.